Towards Elimination of the Dark-Rim Artifact in First-Pass Myocardial Perfusion MRI: Removing Gibbs Ringing Effects Using Optimized Radial Imaging

Behzad Sharif,[1,2] Rohan Dharmakumar,[1,2] Troy LaBounty,[1,3] Reza Arsanjani,[1,4] Chrisandra Shufelt,[4,5] Louise Thomson,[4] C. Noel Bairey Merz,[2,4,5] Daniel S. Berman,[1,2,4] and Debiao Li[1,2,6]

Purpose: Subendocardial dark-rim artifacts (DRAs) remain a major concern in first-pass perfusion (FPP) myocardial MRI and may lower the diagnostic accuracy for detection of ischemia. A major source of DRAs is the "Gibbs ringing" effect. We propose an optimized radial acquisition strategy aimed at eliminating ringing-induced DRAs in FPP.
Theory and Methods: By studying the underlying point spread function (PSF), we show that optimized radial sampling with a simple reconstruction method can eliminate the oscillations in the PSF that cause ringing artifacts. We conducted realistic MRI phantom experiments and in vivo studies ($n = 12$ healthy humans) to evaluate the artifact behavior of the proposed imaging scheme in comparison to a conventional Cartesian imaging protocol.
Results: Simulations and phantom experiments verified our theoretical expectations. The in vivo studies showed that optimized radial imaging is capable of significantly reducing DRAs in the early myocardial enhancement phase (during which the ringing effect is most prominent and may obscure perfusion defects) while providing similar resolution and image quality compared with conventional Cartesian imaging.
Conclusion: The developed technical framework and results demonstrate that, in comparison to conventional Cartesian techniques, optimized radial imaging with the proposed optimizations significantly reduces the prevalence and spatial extent of DRAs in FPP imaging. **Magn Reson Med 72:124–136, 2014. © 2013 Wiley Periodicals, Inc.**

INTRODUCTION

A decrease in myocardial perfusion represents an early marker reflecting the functional effects associated with abnormalities in the coronary arteries (1). In fact, direct visualization of perfusion deficits is the preferred diagnostic test in patients with suspected myocardial ischemia or coronary artery disease. With recent hardware and software improvements, MR myocardial first-pass perfusion (FPP) imaging (2) is emerging as an attractive alternative to the widely available nuclear imaging modalities (3–7). Despite significant technical advances during the past decade, a persistent problem in myocardial FPP imaging—and perhaps the most frustrating one—is the well-known subendocardial dark-rim artifact (5–10).

Dark-rim artifacts (DRAs) are a major drawback for accuracy and widespread adoption of FPP imaging (6,7,11) because they impede diagnosis of hypoperfusion in the subendocardium, which is the most and typically the earliest affected myocardial layer in ischemic disease (12). Specifically, when FPP is used to diagnose patients with mild or moderate levels of hypoperfusion, DRAs may be interpreted as perfusion defects and therefore may reduce the diagnostic specificity. Alternatively, they may reduce the sensitivity if the reader dismisses true deficits as artifacts. Another example highlighting the need for eliminating DRAs is the diagnosis of patients with coronary microvascular dysfunction (13,14), because their perfusion deficits tend to be mild and subendocardial (15,16). Therefore, establishing an acquisition scheme that is robust to DRAs can significantly increase the diagnostic performance of FPP imaging and its clinical use for a variety of patient cohorts.

For qualitative (visual) assessment of FPP, the current approaches for distinguishing artifacts from true deficits (e.g., examining the spatial/temporal characteristics of the artifact or stress-rest comparisons) are subjective and, though potentially helpful (6,17,18), do not provide a systematic solution and are limited due to inherent variability of DRAs (10,19). Furthermore, even if an experienced reader can "read through" DRAs, it could be the case that some subendocardial deficits "fill in"

[1]Biomedical Imaging Research Institute, Cedars-Sinai Medical Center, Los Angeles, California, USA.

[2]Department of Biomedical Sciences, Cedars-Sinai Medical Center, Los Angeles, California, USA.

[3]Department of Medicine, University of Michigan, Ann Arbor, Michigan, USA.

[4]Heart Institute, Cedars-Sinai Medical Center, Los Angeles, California, USA.

[5]Barbra Streisand Women's Heart Center, Cedars-Sinai Heart Institute, Los Angeles, California, USA.

[6]Department of Bioengineering, University of California Los Angeles, Los Angeles, California, USA.

*Correspondence to: Debiao Li, Ph.D., 8700 Beverly Blvd., PACT Ste 800, Los Angeles, CA 90048. E-mail: debiao.li@cshs.org

early while the DRA is still present—that is, during the early myocardial enhancement phase (7). This will inevitably result in missed or misread perfusion defects. Moreover, in quantitative perfusion assessment, the DRA problem is even worse and may result in significant errors (11).

DRAs have been linked to multiple factors, including: Gibbs ringing or truncation artifact (9), cardiac motion (20), susceptibility effects from contrast dynamics (21–23), and signal variation during acquisition (6). Recently, there have been several attempts at minimizing DRAs, mainly by improving the spatial resolution using temporally accelerated reconstruction–for example, using model-based (so called "k-t") (24–27) or compressed sensing techniques (28–30). The attempts at decreasing DRAs based on increased spatial resolution is motivated by minimizing the "Gibbs ringing" effect that is thought to be a central source of DRAs (7,9). Gibbs ringing is a fundamental property of practical Fourier imaging systems, because the underlying spectrum (k-space data) has infinite support but is approximated by a finite number of samples (31,32). The ringing phenomenon refers to oscillations in the reconstructed image intensity that include signal dips (undershoot) at sharp image edges (e.g., the left ventricle [LV] cavity–endocardium boundary), which may manifest as the DRA (9). In this study, we focus on the contribution of Gibbs ringing to DRAs and propose a radial imaging strategy that effectively eliminates ringing-induced artifacts. The underlying theory is inspired by results from classical CT and tomographic reconstruction literature (33), which show that projection imaging with a high resolution exhibits minimal Gibbs-like ringing artifacts (34).

Our first objective is to design and optimize a radial sampling scheme that, combined with a simple reconstruction scheme, is virtually free of ringing-induced artifacts. Based on theoretical derivations combined with numerical and imaging verifications, we show that optimized radial imaging with wide k-space coverage can effectively remove Gibbs ringing effects. The second objective of this work is to evaluate whether radial imaging using our proposed optimized scheme will significantly reduce the prevalence and spatial extent of DRAs in FPP imaging compared with the conventional Cartesian technique, while providing equivalent resolution and similar image quality.

THEORY

Preliminaries

We use the following terminology and notations in connection with Cartesian and radial sampling schemes. We denote the number of readouts by N_{RO} and the number of samples per readout by N_S The field of view (FOV) along the "readout direction" (x or r for Cartesian and radial sampling, respectively) is assumed to be the interval [-L,L] for a fixed L>0. Therefore, the readout resolution (for either scheme) is proportional to N_S In Cartesian and radial k-space, the readout dimension is denoted by k_x and k_r, respectively, and the sampling interval along read-

out Δk is assumed to satisfy the conventional two-fold oversampling (relative to the Nyquist criterion) used in modern MR scanners—namely, $\Delta k < 1/4L$. In case of Cartesian sampling, we refer to "readouts" to denote the phase-encoding (PE) lines, "readout resolution" to represent the resolution along the frequency encode (FE) direction, and "samples per readout" to be the number of FE samples. In general, the spatial resolution along a certain dimension is proportional to the maximum sampled frequency along the corresponding k-space dimension, denoted by adding a superscript max to the k-space dimension. Specifically, $k_y^{\max} = N_{RO}\Delta k/2$ determines the PE resolution, and the readout resolution for Cartesian and radial sampling are determined by $k_x^{\max} = N_S\Delta k/2$ and $k_r^{\max} = N_S\Delta k/2$, respectively. Finally, we assume uniform sampling between the readouts—that is, uniform PE spacing $(1/\text{FOV}_y)$ for the Cartesian scheme and uniform angular sampling for the radial scheme.

Point Spread Function Analysis: Sufficiently Sampled (Ideal) Scenario

We studied the differences in the general properties of Cartesian and radial k-space sampling schemes, focusing on the components that contribute to ringing artifacts in the acquired images. A classical method for describing the effect of different sampling patterns in imaging is to characterize the corresponding point spread function (PSF) (35). Given the PSF corresponding to a k-space sampling pattern, the reconstructed image is the result of two-dimensional (2D) convolution of the PSF with the magnetization density (i.e., the ground-truth image). Figure 1a depicts an example of isotropic-resolution Cartesian and radial sampling patterns with the same resolution ($k_x^{\max} = k_y^{\max} = k_r^{\max}$).

To study the Cartesian acquisition scheme, we calculated the PSF for a Nyquist-sampled Cartesian pattern with N_{RO} readouts (PEs) and N_s samples per readout (FEs). Without loss of generality, we assume $N_{RO} = 256$ and $N_s = 192$. The FOV along y is assumed to be 25% smaller, yielding a rectangular FOV, which is typically used in Cartesian imaging. The PSF is numerically approximated by 20-fold zero-padding of an all-unity k-space matrix of 256×192 (equivalent to the underlying image being a 2D Dirac delta function) and computing the 2D inverse discrete Fourier transform. The resulting real-valued image is then scaled (peak value normalized to 1) to yield the PSF in (x, y) domain. Figure 1b1 shows the absolute value of the computed 2D PSF for the described Cartesian scheme (two-fold zoom). The analytical PSF expression for 2D Cartesian sampling is the well-known 2D periodic *sinc* function (36), which is also called the Dirichlet kernel (31):

$$\text{PSF}_C(x, y) = \Delta k^2 \frac{\sin\left(2\pi x k_x^{\max}\right)}{\sin\left(\pi x \Delta k\right)} \frac{\sin\left(2\pi y k_y^{\max}\right)}{\sin\left(\pi y \Delta k\right)} \quad [1]$$

Figure 1b2 shows a one-dimensional (1D) cut of the PSF along the y, which coincides with the x-axis cut (consistent with Eq. [1]). If convolved with a 2D image
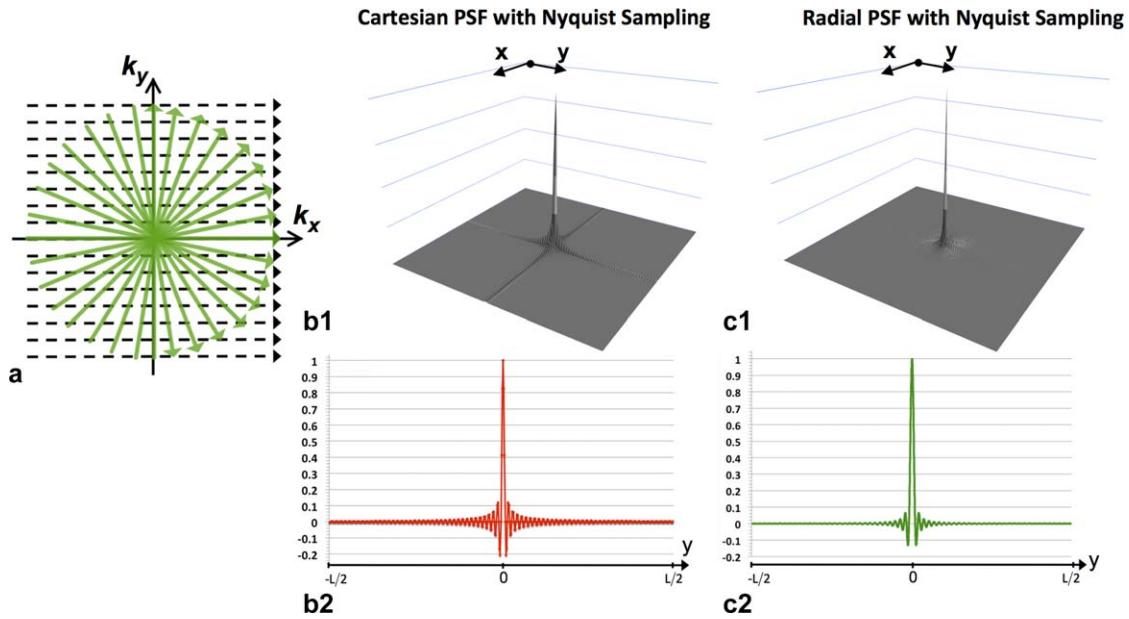
FIG. 1. PSF analysis for the sufficiently sampled scenario. **a:** Schematic for sufficiently sampled Cartesian and radial sampling patterns with the same readout resolution. **b1, c1:** Absolute value of the PSFs for Nyquist-sampled Cartesian and radial acquisitions, respectively (with $N_S = 256$ samples per readout and a fixed FOV of [-L,L]). **b2, c2:** 1D cuts of the respective PSFs along the *y* axis (same as the cut along *x* axis). [Color figure can be viewed in the online issue, which is available at wileyonlinelibrary.com.]

with sharp edges (e.g., bloodpool-myocardium border in FPP images), these oscillations will result in image artifacts, referred to as Gibbs ringing artifacts. In effect, signal values around the image edge are modulated by the positive/negative side-lobes of the PSF, resulting in reconstructed intensities above/below the ground truth.

Next, we compute the PSF for a radial acquisition scheme with the same readout resolution ($N_s = 256$) and

$N_{RO} = 402$ readouts (projections), which matches the requirement for zero angular aliasing according to the Nyquist criterion (33). The radial PSF is computed as follows: (1) sampling a uniform (all unity) k-space along the described radial trajectory; (2) regridding the sampled data using a conventional Kaiser-Bessel gridding kernel (width 4) and density compensation function (DCF); and (3) scaling the resulting real-valued image
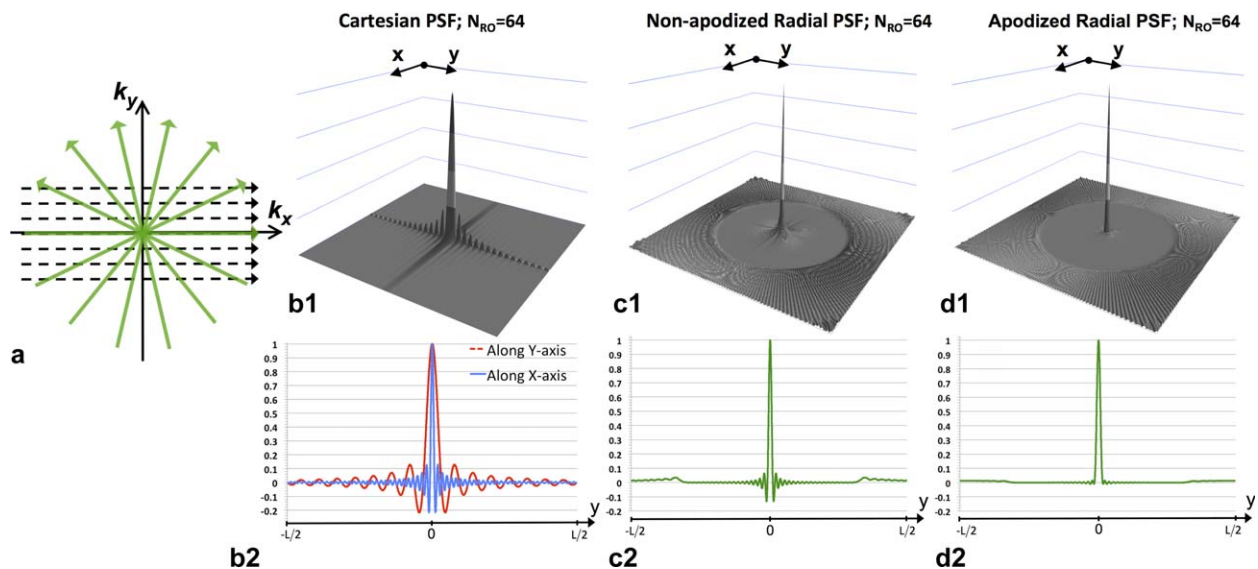

FIG. 2. PSF analysis for the limited readouts scenario. **a:** Schematic for the limited readout sampling scenario for Cartesian and radial acquisition with equal number of readouts and readout resolution. **b–d:** PSFs with $N_{RO} = 64$ readouts and $N_S = 256$ samples per readout (fixed readout FOV [-L,L]). **b1, b2:** Absolute value of the Cartesian PSF and its 1D cuts along *x* and *y*; the FOV along the PE line is [-0.75L, 0.75L]. **c1, c2** and **d1, d2:** Radial PSF and its 1D cut corresponding to nonapodized reconstruction and apodized reconstruction (apodizer as in Eq. [3] using $\Omega = 1.17$), respectively. In contrast to radial sampling, insufficient k-space coverage along k_y (PE) in Cartesian sampling results in low-frequency oscillations along *y* (three-fold wider side lobes than *x*), as shown in panels b1 and b2. [Color figure can be viewed in the online issue, which is available at wileyonlinelibrary.com.]

(peak normalized to 1). This conventional DCF is ramp-shaped and equal to $|k_r|$ (except for the origin), which hereafter is referred to as the "ramp DCF" (37). The corresponding PSF (absolute value) is shown in Figure 1c1. The analytical formula describing the behavior of this circularly symmetric PSF in (r, θ) polar coordinates can be written as:

$$\text{PSF}_R(r) \approx \frac{\pi(\Delta k)^2}{4} + (2k_r^{\max})^2 \text{jinc}(2k_r^{\max} r) \qquad [2]$$

where $\text{jinc}(r) = J_1(\pi r)/2r$, in which $J_1(r)$ is the first-order Bessel function (38). This radially symmetric function has been described before in the MR literature by Lauzon and Rutt (39) using classical results from radio astronomy (40). The *jinc* function in Eq. [2] is the analog of *sinc* (Eq. [1]) in 2D polar coordinates and is equal to the spectrum (Hankel transform) of a unit-height disk (38,40). Note that the PSF depicted in Figure 1c1 does not exactly conform to Eq. [2] because of the effects of higher order terms in the PSF located at multiples of $1/\Delta k$ in addition to underlying numerical errors. However, these effects are negligible for the described sampling scheme, and Figure 1c1 closely follows $|\text{PSF}_R(r)|$ because the effect of higher order terms is negligible for a small enough readout sampling interval Δk, satisfying $\Delta k < 1/4L$. [Specifically, this condition ensures that the "polar ring" components of the radial PSF can be ignored in the imaged FOV (39).] Figure 1c2 shows a 1D cut of the real-valued PSF along y. Similarly to Cartesian imaging, the PSF consists of a narrow main lobe and oscillating side lobes, which may also result in ringing artifacts when convolved with the underlying image; this effect is sometimes referred to as "radial ringing" in MRI literature (39) or as the "Airy pattern" in Fourier optics (38).

For both Cartesian and radial schemes, the frequency (spatial density) of PSF oscillations is proportional to the resolution (Figure 1b2 and 1c2). Consequently, any potential ringing-induced DRAs become more compact and therefore visually less significant (9,10). However, a key difference between Cartesian and radial schemes is that the oscillation frequency for radial PSF in both x and y directions only depends on the readout resolution, $k_r^{\max}$, which is proportional to N_s. In contrast, the frequency of oscillations along y for the Cartesian PSF is a function of the PE resolution, $k_y^{\max}$, which is proportional to N_{RO}. Therefore, increasing the oscillation frequency of the underlying PSF for radial imaging comes with almost no acquisition time penalty (since it only requires increasing N_s for a fixed FOV), whereas accomplishing the same for Cartesian imaging may incur significant acquisition time penalty, since it requires increasing N_{RO} (i.e., more readouts). In addition to the oscillation frequencies, there are other differences between the characteristics of the PSFs shown in Figure 1 (Eqs. 1 and 2), which include the peak amplitude and decay rate of the side lobes, both of which are more desirable for the radial PSF (38,41). However, these differences correspond to 1D cuts of the PSFs, and their effects on the reconstructed image are difficult to analyze analytically. Consequently, we used numerical simulations to study such differences (see the Methods section).

PSF Analysis: Limited Readouts (Practical) Scenario

Figure 2 describes the PSF properties of Cartesian and radial acquisitions for a practical scenario wherein only a limited number of readouts is acquired, while the readout resolution is the same as before ($N_s = 256$ samples). The schematic for this "limited readouts" scenario is depicted in Figure 2a. In contrast to the previous section (the "sufficiently sampled" scenario in Figure 1), here we assume that the same number of readouts N_{RO} is acquired for both Cartesian and radial sampling schemes. Without loss of generality, in the following we assume $N_{RO} = 64$. For Cartesian imaging, given the rectangular FOV (25% reduced FOV along PE), this sampling scheme implies a 3-to-1 resolution difference between x and y dimensions ($k_y^{\max} = k_x^{\max}/3$). The corresponding PSF and 1D cuts are shown in Figures 2b1 and 2b2, respectively. The Cartesian PSF oscillations along y have a three-fold lower frequency compared with the one in Figure 1b2 with similar peak side-lobe amplitudes. The wider main lobe along y implies lower spatial resolution; more importantly, the wider side lobes yield a wider (more spatially prominent) ringing artifact.

In the following, we refer to conventional regridding reconstruction of radial acquisition using the ramp DCF as "nonapodized" reconstruction. The computed nonapodized radial PSF and its 1D cut are shown in Figure 2c1 and 2c2 and correspond to nonapodized regridding reconstruction of $N_{RO} = 64$ projections. Figure 2c1 matches the previous description in the literature (42,43): the PSF for angularly undersampled radial acquisition consists of a superposition of the principal *jinc* component and its associated side lobes (Fig. 1c1 and 1c2) plus the "streaking" components that start outside of a certain radius. This radius for the described sampling scheme is approximately 0.3L, i.e., 15% of the FOV; also, the peak amplitude of the streaking components is located at 0.35L and has a value of 3.4%. In comparison, the peak negative and positive side lobe amplitudes (*jinc* component) of this PSF are -13.2% and 6.4%, respectively, which is the same as the sufficiently sampled radial PSF in Figure 1. The key observation in comparing the limited-readout radial scheme in Figures 2c1 and 2c2 with the sufficiently sampled one in Figures 1c1 and 1c2 is that both PSFs show almost identical oscillatory (*jinc*) components.

Comparing the radial and Cartesian sampling schemes in Figure 2, it is worth emphasizing that the total acquisition time is the same between the two (note that $N_{RO} = 64$ is fixed and that $k_x^{\max} = k_r^{\max}$). However, the radial trajectory samples the high-frequency k-space regions in all directions, yet the Cartesian trajectory misses some of the high frequency regions specifically along the PE direction, which results in low-frequency oscillations in the PSF along y. Hence, the expected ringing artifact for radial sampling (with nonapodized reconstruction) is expected to be less significant (i.e., narrower) compared with Cartesian sampling (along PE) (44).

PSF Analysis: Radial Imaging with Optimized Apodization

The PSF for radial imaging also depends on the reconstruction method used, i.e., the PSF corresponding to

nonapodized reconstruction (discussed above) is different from the one corresponding to filtered backprojection or regridding reconstruction incorporating apodization (41,45). Here, we consider the radial PSF corresponding to regridding reconstruction using an apodized k-space weighting instead of the nonapodized ramp-shaped DCF. We use a Gaussian kernel as the "apodizer" (apodizing function) with the following form:

$$A(k_r) = \exp\left(-\pi\left(\frac{k_r/k_r^{\max}}{\Omega}\right)^2\right) \qquad [3]$$

for some pre-defined parameter Ω. In the apodized reconstruction, the radial readouts are first multiplied by $A(k_r)$, which reduces the weighting of high-frequency k-space samples, before conventional density compensation (i.e., weighting by the ramp-shaped DCF) and regridding. The typical motivation for using an apodized reconstruction in projection imaging is to achieve high-frequency noise suppression to improve signal-to-noise ratio (SNR), which comes at the expense of reduced effective resolution (35,37). The equivalent image-domain operation for the described Gaussian apodization is smoothing by a 2D circularly symmetric Gaussian kernel. It can be shown that the effective full width at the half maximum (35) of the underlying PSF will increase with decreasing Ω, thereby reducing the effective isotropic resolution. Note that because $k_r^{\max}$ is the same for the apodized scheme, the PSF oscillation frequency will stay the same, but the amplitude of oscillations can be significantly suppressed (32) and even effectively eliminated for a small enough Ω.

To apply the apodizer and study its effect of the radial PSF, we first need to choose an *optimal parameter* Ω for the Gaussian kernel in Eq. [3]. Our optimization criterion is to minimize the resolution penalty (reduction factor), i.e., to find the maximal Ω^* such that the peak negative side lobe of the resulting PSF will be lower than 1% (i.e., an apodizer that essentially eliminates all ringing components [side lobes] from the PSF). The Gaussian apodizer in Eq. [3] can be shown to be *near optimal* in the sense of providing maximum suppression in the amplitude of the largest side lobe for a given resolution penalty. The proof is beyond the scope of this study, but a related work has been described recently for Fourier spectrometry (46). The result of the numerical search algorithm for the described radial sampling pattern was $\Omega^* = 1.17$ To quantify the effect of the corresponding apodization on the reconstructed resolution, we compared the FWHM of the main lobe of the resulting PSF to that of the nonapodized PSF in Figure 2c1. The ratio of FWHMs (apodized over nonapodized) is 1.28, implying a 1.28-fold reduction in effective resolution along x and y.

Figure 2d1 and 2d2 shows the radial PSF corresponding to the same sampling scheme as in Figure 2c1 and 2c2 but using the optimized apodized reconstruction instead of the nonapodized reconstruction. As seen in the 1D cut shown in Figure 2d2, we have eliminated almost all ringing components (peak negative amplitude = −0.95%, 14 times smaller than Figure 2c2) and significantly reduced the streaking components

(peak streak amplitude = 1.3%, 2.6 times smaller than Figure 2c2). Therefore, in addition to improving SNR, the apodized reconstruction reduces streaking and effectively eliminates oscillations in PSF (source of ringing artifacts) at the cost of reduced resolution. An acquisition scheme that samples the data at this reduced resolution and does not use apodization is more SNR-efficient (compared with the apodized scheme) but will not achieve the desired reduction of the ringing components. In practice (and as described in the Methods and Results sections), given a desired spatial resolution for the reconstruction, this trade-off (resolution versus ringing) can be flexibly adjusted using the described Gaussian apodizer.

METHODS

Numerical Simulation

The PSF properties described in the Theory section were verified by simulating k-space sampling and reconstruction for a noise-free numerical phantom consisting of two overlapping inner/outer disks (Fig. 3, top row) with the following specifications: ratio of inner to outer disk radius $= R_{in}/R_{out} = 2/3$ and signal intensity ratio between the two disks was 6:1, which represents a maximal ("worst case") contrast ratio along the subendocardial border for FPP. We used the same Cartesian and radial sampling patterns as in Figure 2. To compute the k-space data samples accurately for a given sampling pattern, we applied the following analytical expression for $D(k_r)$, the circularly symmetric 2D Fourier representation of the described phantom (36,38):

$$D(k_r) = 10\pi \cdot R_{in}^2 \frac{J_1(k_r R_{in})}{k_r R_{in}} + 2\pi \cdot R_{out}^2 \frac{J_1(k_r R_{out})}{k_r R_{out}} \qquad [4]$$

Phantom Experiment

To verify the theoretical assertions, an MR phantom intended to simulate a geometrically-realistic FPP scenario with worst-case signal intensity variations (similarly to the numerical phantom above) was designed. The phantom was composed of multiple regions of interest (ROIs) made of gelatin and saline doped with various concentrations of a Gadolinium-based contrast agent (gadoversetamide), and surrounded by two bottles. Figure 4 shows the result of a fully sampled scan of the phantom, which was used as the "ground truth" image. The phantom was intended to resemble the left ventricle (ROIs: "LV cavity" region, "normal" region, "deficit" region) during the wash-in phase of the contrast agent, and the bottles were to represent the surrounding tissue. Further details including T1 values are included in the Figure 4 caption.

MR data was acquired on a 3T clinical scanner (Magnetom Verio; Siemens Healthcare, Erlangen, Germany) with a standard cardiac-torso receiver array. The scan parameters used to image the phantom in Figure 4 (i.e., our ground-truth scan) were as follows: radial FLASH with saturation recovery (SR) preparation; 1.0×1.0 mm^2 resolution; slice thickness: 6 mm; FOV: 384×384 mm^2; 384 projections with 384 samples per readout; number of channels = 15; receiver bandwidth = 650 Hz/pixel; flip angle = 12°; TR/TE = 3.0/1.8 ms; and SR time = 90 ms.
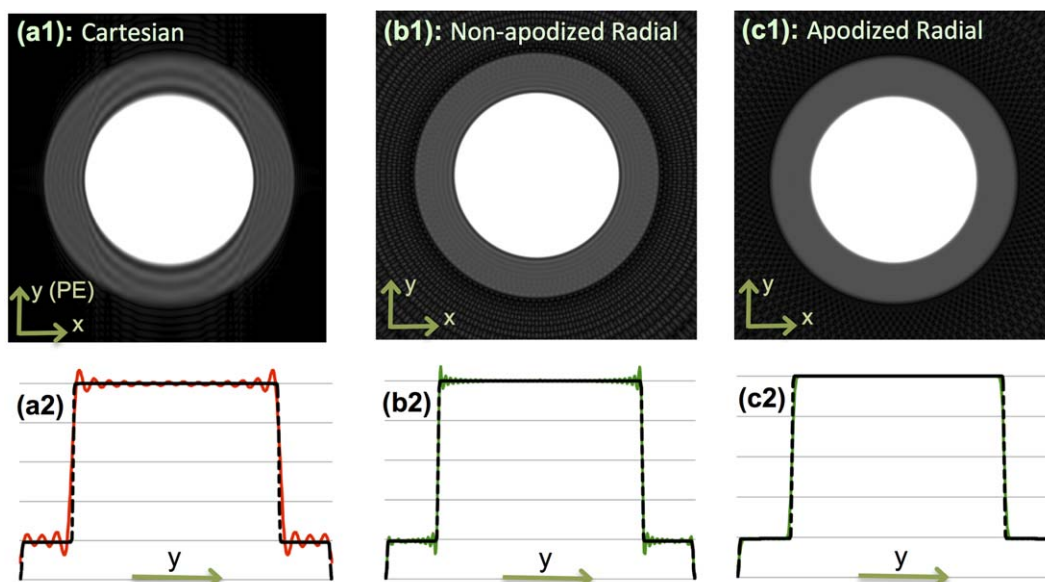
FIG. 3. Numerical phantom results. **a1:** Cartesian reconstruction of analytical disk phantom with same acquisition scheme as in Figure 2 (three-fold lower resolution along *y*). **b1:** Nonapodized radial reconstruction (same number of readouts and readout resolution). **c1:** Apodized radial reconstruction with the same k-space data as in panel b1 (same apodizer as for Figure 2d). All images use zero-filled interpolation to a 512 × 512 image matrix. **a2**, **b2**, and **c2:** 1D cuts of the images in the top panel along the center of the image parallel to the *y* axis that are overlaid on the ground truth (dotted line). The Cartesian image in panel a1 exhibits significant ringing artifacts (Gibbs) along *y* (PE), whereas apodized radial reconstruction in panel c1 eliminates all ringing-induced artifacts and has reduced streaking compared with panel b1. Specifically, the energy (2-norm) of the streak region outside of the disks as a percentage of the energy of the disk phantom is 40% lower in panel c1 compared with panel b1 (11.5% versus 19%). Overall, the results verify the PSF effects described in Figures 1 and 2, and demonstrate that radial sampling with wide k-space coverage and apodized reconstruction can effectively eliminate the DRAs caused by Gibbs-like ringing effects. [Color figure can be viewed in the online issue, which is available at wileyonlinelibrary.com.]

The ratio of the signal intensity in the cavity (ROI #2) to the normal region (ROI #1) was approximately 6:1 (range along the edge: 5.5–6.1). This signal intensity ratio is higher than the typical 5:1 or 3:1 ratio encountered in vivo. However, as stated above, the goal was to test the robustness of radial imaging (with wide k-space coverage) to ringing artifacts, and as such, the 6:1 ratio represents a worst-case scenario.

We conducted Cartesian and radial phantom scans using Cartesian/radial SR-prepared FLASH pulse sequences. Both datasets were acquired using $N_{RO} = 77$ readouts with $N_s = 256$ samples per readout and similar sequence parameters as the ground truth scan above. Consequently, the acquired readout resolution for both datasets was 1.5 mm. The Cartesian scan used a rectangular FOV of 384 × 230 mm^2 (PE resolution: 3.0 mm). Two reconstructions were performed from the radial dataset: (1) nonapodized (k-space data only weighted by ramp DCF before regridding); and (2) Gaussian-apodized (data also weighted by the optimized Gaussian kernel before DCF weighting and regridding). All radial/Cartesian reconstructions used sum-of-squares coil combination followed by standard zero-filled interpolation to a 512 × 512 image matrix [to minimize variability to subpixel shifts (10)].

In Vivo Studies

Following informed consent, healthy human volunteers (n = 12; 7 women, 5 men; average age = 24 years) with no history of heart disease or diabetes were imaged on the same 3T scanner according to a study protocol approved by the Institutional Review Board at Cedars-Sinai Medical Center. Two FPP scans, both using SR-prepared FLASH acquisition, were performed at rest (breathhold scans during 50 heartbeats; mean scan time = 42 s) using an optimized radial pulse sequence followed by the product FPP Cartesian sequence (see details below), with a 10- to 12-minute time gap between the two scans to allow for contrast washout. The contrast injection dose (gadoversetamide) for each perfusion scan was 0.04 mmol/kg. All scans were "single shot" (i.e., there was no data sharing between heartbeats), and the number of readouts were matched between the radial and Cartesian scans within ±3 readouts (range: 48–56). The readout resolution for the Cartesian scans was matched to that of the radial scan (range: 1.8–1.9 mm; average = 1.8 mm; the reconstructed resolution for radial images was different, as described below), and the PE resolution was 2.7–2.9 mm (average = 2.8 mm). The parameters for the Cartesian scan (product sequence) were as follows: FOV read = 270–350 mm; flip angle = 12°; 15 receiver channels; receiver bandwidth ≈680 Hz/pixel; TR = 2.5–2.6 ms; TE = 1.3–1.4 ms; SR time = 100 ms with linear PE ordering; three contiguous slices per heartbeat (8 mm thickness, centered at midventricle), each acquired following a composite (product) SR preparation pulse train (6); TGRAPPA rate 2; online image reconstruction on the scanner. The radial FPP scans used a customized pulse sequence with similar
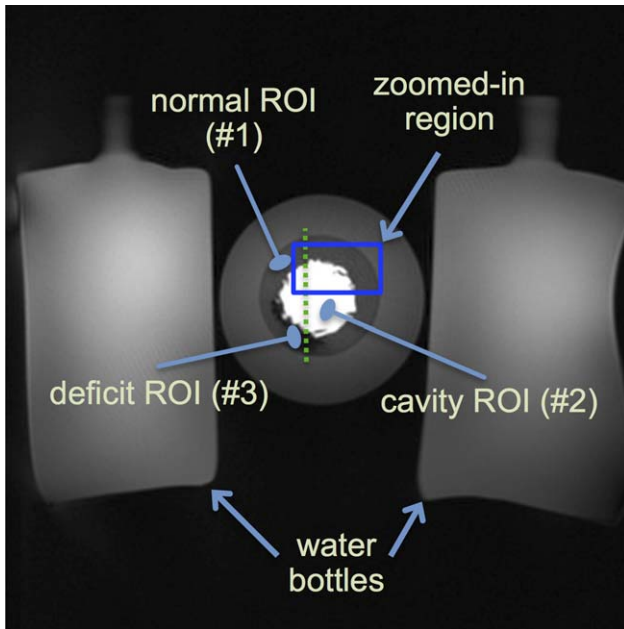
FIG. 4. Description of imaged MR gelatin-Gadolinium phantom with realistic signal intensity ratios, used to demonstrate robustness of projection imaging to Gibbs ringing. This "ground truth" image is acquired at 1.0×1.0 mm^2 resolution using an SR-prepared FLASH radial pulse sequence with 384 readouts (projections). The ratio of the signal intensity in the cavity (ROI #2) to the normal region (ROI #1) is approximately 6:1 (range, 5.5–6.1). The cavity and normal regions were composed of a mixture of gelatin, saline, and contrast whereas the deficit region (ROI #3) contained almost no contrast agent. The T1 values ROI #1, #2, and #3, are approximately 750 ms, 60 ms, and 1200 ms, respectively (estimated based on pixel-by-pixel T1 fitting using Cartesian data acquired separately with six different inversion times). The highlighted box is the zoomed-in region shown in Figure 5. The dotted line shows the location of the cut for the 1D profiles shown in Figure 5. [Color figure can be viewed in the online issue, which is available at wileyonlinelibrary.com.]

parameters except the following: a fixed FOV of 285 mm (two-fold readout oversampling with 320 samples/spoke) and a BIR-4 adiabatic 90° pulse for SR preparation prior to acquisition of each slice. Due to the SAR limitations of the employed BIR-4 pulse at 3T, we anticipated that we will be limited to acquisition of two slices per R-R interval for some of the subjects and therefore scanned one slice position (midventricular) two to three times per heartbeat in all radial scans. The motivation for using a BIR-4 SR pulse was to minimize B_1 inhomogeneities (6,47); nevertheless, the composite SR pulse train (product sequence used in Cartesian scans) has been shown to perform almost as well in the LV region for Cartesian imaging at 3T (48).

The radial pulse sequence included gradient-delay correction [prospectively optimized for the scanner (49)], and acquisition of the radial spokes was eight-fold interleaved to minimize "smearing" artifacts caused by T1 relaxation after the SR pulse (29,50). The interleaving pattern was implemented by first partitioning the total number of spokes (48 or 56) into eight uniformly spaced subsets labeled from G_1 to G_8. The acquisition order for these disjoint groups (each containing seven to eight spokes) was as follows: $\{G_1, G_5, G_3, G_7, G_2, G_6, G_4, G_8\}$.

To further reduce the effects of T1 relaxation and similarly to the KWIC scheme (51), the central k-space data used in the reconstruction was limited to the spokes in the middle of the acquisition window (i.e., $\{G_7, G_2\}$). Specifically, 15 central k-space samples (the DC sample and seven samples on each of its two sides) for spokes in $\{G_3, G_6\}$ and 27 central k-space samples for $\{G_1, G_5, G_6, G_4, G_8\}$ were excluded in the reconstruction (the DCF was adjusted accordingly). In addition, the radial readout direction (polarity) was alternated within each shot to reduce potential off-resonance effects (52). Coil sensitivity profiles were computed by applying an eigenvector-based estimation method (53).

Image Reconstruction and Analysis

Image reconstruction for radial acquisitions was done on a frame-by-frame basis (no temporal acceleration) using non-Cartesian SENSE and performed offline on a workstation (Pentium Dual-Xeon 3.3 GHz) in MATLAB (Mathworks, Natick, Massachusetts) employing 12 computing cores (reconstruction time: 75 s/slice). The reconstruction algorithm was according to a conjugate-gradient scheme with no explicit regularization (54) and employing the Gaussian apodizer (Eq. [3]). The kernel parameter Ω for the apodizer was chosen on the basis of the desired in-plane reconstructed resolution, which was set at 2.15×2.15 mm^2. Given that the acquisition resolution was 1.8 mm (isotropic in-plane), we determined that the apodization should correspond to a 1.2-fold reduction in resolution along each dimension (1.2-fold increase in FWHM of the PSF). We then used the computational framework described in the Theory section (Fig. 2) and selected $\Omega = 1.24$ to yield the desired apodizer. Compared with the apodized radial PSF discussed in the Theory section, the peak negative PSF side lobe amplitude for this setup is -1.6% and therefore is expected to have negligible ringing components, similarly to Figures 2d1 and 2d2.

One representative midventricular image from each radial/Cartesian FPP image series (a total of 24 images for the 12 subjects) was selected from the "early myocardial enhancement" phase (defined as 8 R-R cycles after initial LV cavity enhancement). All representative images were visually scored for artifact by two expert readers blinded to the study protocol using a consensus scoring scheme of 0–4 (0: no artifact; 1: negligible; 2: mild; 3: moderate; and 4: severe artifact). For the radial images, the reconstructed frame (among the two to three frames per R-R cycle) that best matched the Cartesian midventricular image in terms of cardiac phase was chosen for the blind read (to "equalize" the motion effects in the visual comparison as much as possible). The following procedure was used for quantitative scoring of the artifact. Radial reconstructions were converted to DICOM images (using the scanner-produced tags) and imported in an expert viewer (Osirix; Pixmeo, Geneva, Switzerland). For quantitative evaluation, we estimated the spatial width of the DRA in each representative image as a surrogate measure for its severity (24). In particular, spatial widths of the DRAs were computed from the interpolated DICOMs as a measure of the maximal length (largest transmural extent) of the signal dips along
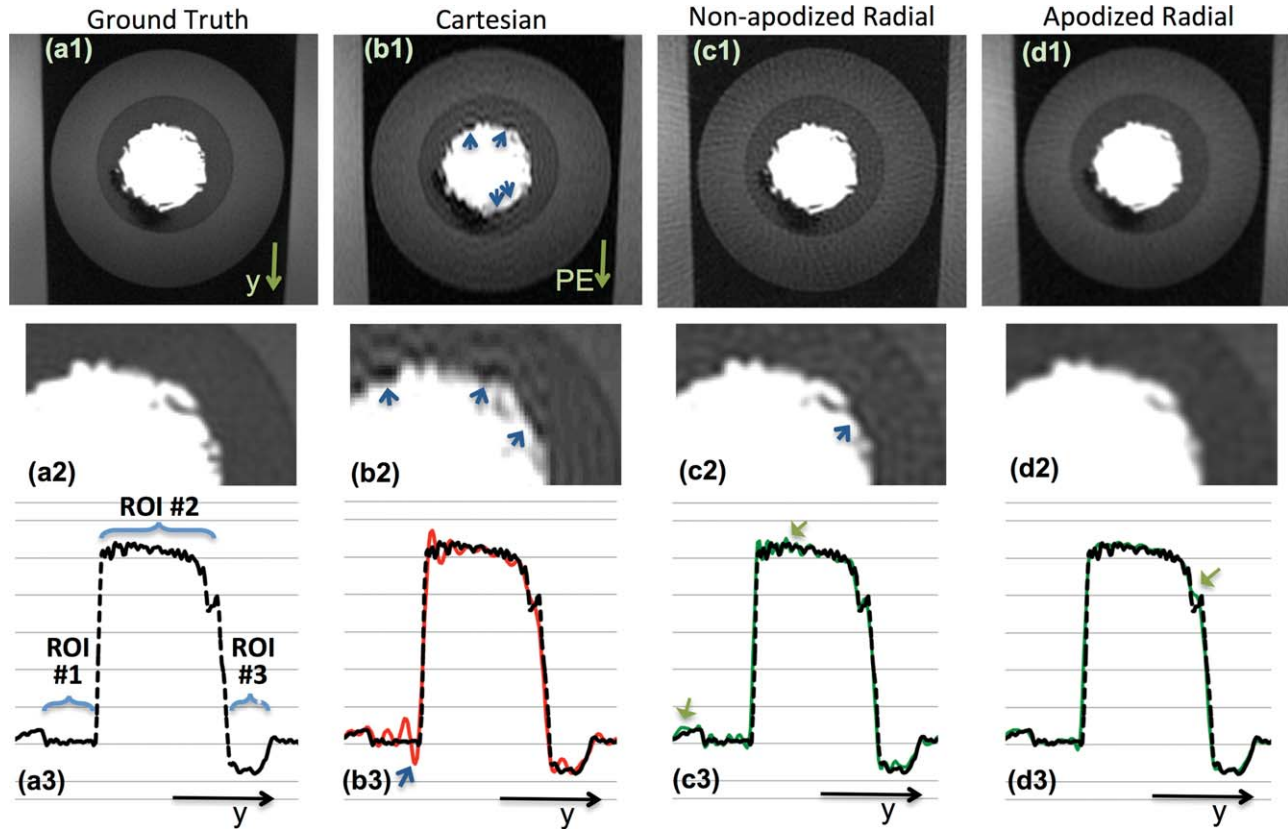
FIG. 5. Reconstruction results for the MR phantom in Figure 4. The top row (**a1–d1**) shows zoomed-in reconstruction result; the middle row (**a2–d2**) shows images in the top row further zoomed-in to the box in Figure 4, and the bottom row (**a3–d3**) shows 1D cuts along the cut line in Figure 4, with panel a3 overlaid on panels b3–d3 for comparison (ROIs in panel a3 are defined in Figure 4). **a1–a3:** Ground truth image with 1.0×1.0 mm^2 resolution. All other panels correspond to reconstructions with 77 readouts (256 samples each). **b1–b3:** Cartesian reconstruction with $1.5 \times 3.0 = 4.5$ mm^2 resolution (FOV size $= 384 \times 230$ mm^2); the arrows in panels b2 and b3 indicate DRAs. **c1–c3:** Nonapodized radial reconstruction with $1.5 \times 1.5 = 2.25$ mm^2 resolution; the arrow in panel c2 points to a negligible DRA, and the arrows in panel c3 show mild streaking. **d1–d3:** Apodized radial reconstruction (same apodizer as Figs. 2d and 3c) with $1.92 \times 1.92 = 3.7$ mm^2 resolution (no DRAs, negligible streaking); the arrow in panel d3 points to over-smoothening of a small feature, which is a consequence of the lower resolution compared with the ground truth in panel a3.

all polar directions (along rays starting from the cavity center and extending toward the endocardium). All statistical tests comparing radial and Cartesian results used the Mann-Whitney U test (equivalent to Wilcoxon rank-sum test) computed in MATLAB (55).

RESULTS

Numerical Simulation

Figure 3 presents the simulation results for the disk-shaped numerical phantom. The top row (Fig. 3a1–3c1) shows the reconstructed images corresponding to the PSFs in Figures 2b1, 2c1, and 2d1, respectively. The lower panels (Fig. 3a2–3c2) show a 1D cut along y, which is overlaid on top of the ground truth (dotted line). As seen from the figure, the nonapodized radial reconstruction yields negligible (very thin) ringing, and the Gaussian-apodized reconstruction completely eliminates any ringing artifact, although at the cost of lower resolution. Specifically, the width of the DRA caused by Gibbs ringing in Figure 3a1 is approximately 17% of the width of the outer disc. In contrast, this measure is 5% for the nonapodized radial reconstruction in Figure 3b1,

and is zero for the apodized reconstruction (with $\Omega = 1.17$) in Figure 3c1. Moreover, the apodized reconstruction has less streaking. Further details are provided in the figure caption. In summary, the simulation results verify the PSF effects described in the Theory section (Figs. 1 and 2).

Phantom Experiment

The reconstruction results for the MR phantom are shown in Figure 5. The first column (Fig. 5a1–5a3) shows the ground truth image (from Figure 4) with 1.0×1.0 mm^2 resolution. All other panels correspond to reconstructions of $N_{RO} = 77$ readouts with $N_s = 256$ samples per readout. The top row (Fig. 5a1–5d1) shows cropped reconstruction results for each acquisition/reconstruction method. Zoomed-in versions of the images (highlighted box in Figure 4) are shown in the middle row (Fig. 5a2–5d2). The bottom row (Fig. 5a3–5d3) shows 1D cuts of the images in the top row. The second column (Fig. 5b1–5b3) shows the Cartesian reconstruction with $1.5 \times 3.0 = 4.5$ mm^2 resolution; arrows in Figure 5b2 and 5b3 point to DRAs. The third
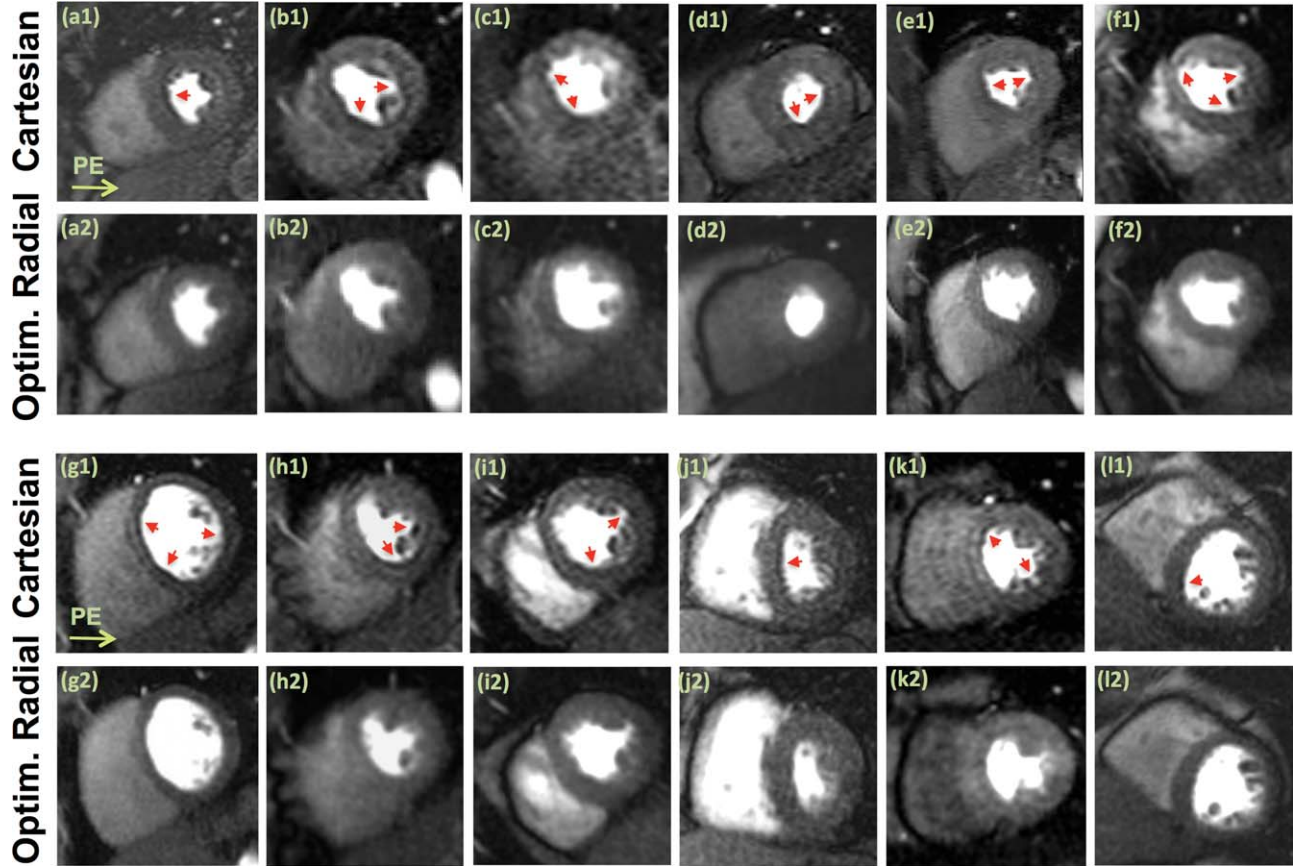
FIG. 6. Representative first-pass myocardial perfusion images (midventricular slice) from each of the 12 healthy volunteer studies; all images correspond to a similarly selected early myocardial enhancement phase (defined as eight R-R cycles after initial LV cavity enhancement). The first row in each panel (**a1–f1** in the top panel and **g1–l1** in the bottom panel), shows Cartesian images (PE direction from left to right). The second row in each panel (**a2–f2** in the top panel and **g2–l2** in the bottom panel) shows the corresponding images for the optimized radial imaging scheme. For the radial images, the reconstructed frame (among two to three midventricular frames in one R-R cycle) that best matched the midventricular Cartesian image in terms of cardiac phase is shown. Arrows point to the observed DRAs. No noticeable DRA is seen in the radial images (although panel e2 shows mild streaking in the septum). Examples of qualitative artifact scores are as follows: panels a1 and a2, Cartesian $= 3.5$, radial $= 0$; panels i1 and i2, Cartesian $= 3$, radial $= 1$. The SNR in the myocardium (mean intensity divided by standard deviation in a homogeneous region at peak enhancement) is similar between Cartesian and radial images (Cartesian, 10.4 ± 2.5 versus radial, 11.7 ± 2.2; $P = 0.40$).

column (Fig. 5c1–5c3) shows the nonapodized radial reconstruction with $1.5 \times 1.5 = 2.25$ mm^2 resolution. The arrow in Figure 5c2 points to negligible (very thin) DRA, and those in Figure 5c3 show mild streaking artifacts. Finally, the fourth column (Fig. 5d1–5d3) shows the apodized radial reconstruction (apodizer as in Eq. [3] using $\Omega = 1.17$) with $1.92 \times 1.92 = 3.7$ mm^2 resolution. This is somewhat better than the overall Cartesian resolution (4.5 mm^2). More importantly, Figure 5d1 exhibits no discernable DRAs and has negligible streaking. The arrow in Figure 5d3 points to a small feature, which is somewhat over-smoothened compared with the ground truth in Figure 5a1–5a3 because of the lower resolution. Note that a similar resolution limitation is seen in the Cartesian image (Fig. 5b3) for reconstruction of the same feature. To quantitatively evaluate the image quality differences in Figure 5, we computed the relative contrast difference between the normal ROI (#1 in Figure 4) and deficit ROI (#3 in Figure 4) as a percentage of the normal ROI. This relative contrast for the ground truth

image (Fig. 5a1), Cartesian image (Fig. 5b1), nonapodized radial image (Fig. 5c1), and apodized radial image (Fig. 5d1) are 79.3%, 68.1%, 70.3%, and 74.5%, respectively.

In Vivo Studies

Representative images from all volunteer studies ($n = 12$) are shown in Figure 6. The image quality in terms of the measured myocardial SNR for the radial and Cartesian images is similar (Cartesian: 10.4 ± 2.5 versus radial: 11.7 ± 2.2; $P = 0.40$); however, unlike the Cartesian images, the reconstructed radial images (optimized scheme) are free of noticeable DRAs. Examples of scores and further details are provided in the figure caption. Figures 6a1–6a2 and Figures 6e1–6e2 correspond to large heavyset subjects (>110 kg). Figure 6e2 shows mild streaking (the only radial FPP image with noticeable streaking in the heart region among the 12 studies), but Figure 6a2 does not. The corresponding movies of the FPP image series for the volunteer studies in Figures 6a1
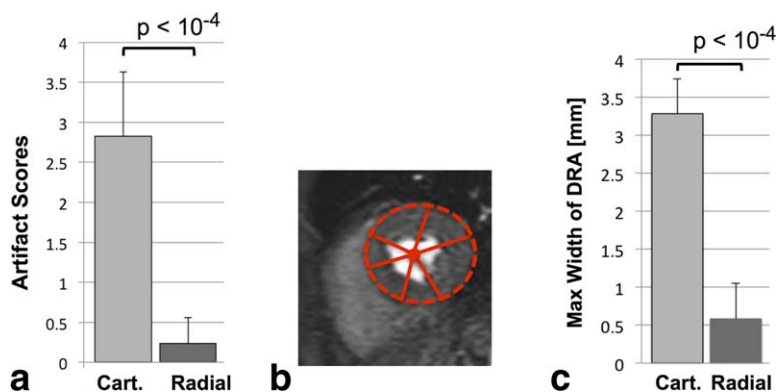
FIG. 7. **a:** Summary of artifact scores for the representative first-pass perfusion images (Fig. 6) assigned by two expert readers (consensus 0–4 scale scoring: 0, no artifact; 1, negligible; 2, mild; 3, moderate; 4, severe artifact). The results clearly show the superiority of optimized radial imaging in reducing the DRA (Cartesian, 2.83 ± 0.8 versus optimized radial, 0.24 ± 0.32; $P < 0.0001$). **b:** Quantification scheme for measuring the maximum width (largest transmural extent) of the DRA along angular directions (as explained in the Methods section). **c:** Summary of the DRA width measurements as shown in panel b, indicating that the maximal width of DRA is significantly reduced with optimized radial imaging (Cartesian, 3.28 ± 0.46 versus optimized radial, 0.58 ± 0.47; $P < 0.0001$). Note that quantitative DRA measurements become less accurate for subpixel widths. [Color figure can be viewed in the online issue, which is available at wileyonlinelibrary.com.]

and 6a2 is provided in the Supporting Information available in the online version of this article. Figure 7a shows mean artifact scores assigned by expert readers, clearly indicating superiority of the optimized radial imaging method in reducing the DRA ($P < 0.0001$). Figure 7b depicts the quantification scheme for estimating the DRA width and Figure 7c summarizes the measurements, indicating that the DRA width is significantly reduced for optimized radial imaging ($P < 0.0001$). In summary, the in vivo results show a very significant reduction of the DRA using the optimized radial imaging scheme, both in terms of qualitative scores and quantitative assessment.

DISCUSSION

In this work, we proposed a radial sampling strategy that, based on optimization of the associated point-spread function, eliminates ringing-induced artifacts and hence may enable reconstructing first-pass myocardial perfusion images free of the DRA. For imaging experiments, we developed and applied an optimized FPP imaging technique based on the proposed radial sampling scheme with wide k-space coverage, and a rather simple frame-by-frame reconstruction method (i.e., each frame is reconstructed independent of others and without temporal acceleration) using numerically optimized apodization. We demonstrated the capability of the proposed method through a systematic theoretical description combined with numerical simulations in addition to phantom and in vivo experiments, as summarized in the following:

—First, our study highlighted the fact that, unlike conventional Cartesian sampling, radial sampling has the following property: the frequency of PSF oscillations along both spatial dimensions becomes narrower using a wider k-space readout (i.e., a higher readout resolution or $k_r^{\max}$, equivalent to more samples per readout for a fixed FOV) which implies narrower (i.e., less significant) ringing artifacts for the reconstruction.

—Second, we noted that widening the k-space readout yields negligible temporal resolution penalty (although it results in an expected SNR cost).

—Third, we showed that, with a simple scheme for optimized apodized reconstruction, one can trade off in-plane resolution to simultaneously eliminate the PSF oscillations—hence the associated ringing artifacts—and improve the image quality (thanks to reduced streaking and higher SNR).

—Fourth, and most importantly, using the proposed radial acquisition scheme with typical FPP sequence parameters, the level of apodization needed for achieving the desired PSF behavior (i.e., highly suppressed ringing/oscillatory components) is quite mild and, therefore, implies a benign loss in reconstructed resolution. We specifically chose the apodization parameter (Gaussian kernel in Eq. [3]) such that the effective in-plane resolution of radial images matches or slightly outperforms the typical resolution in conventional Cartesian imaging. For the presented in vivo results (Fig. 6), the radial dataset was acquired at 1.8×1.8 mm^2 resolution and all acquired samples were used in the reconstruction but, by applying the apodizer (Eq. [3]), we reconstructed the images at a lower resolution, namely, 2.15×2.15 mm^2, with almost no ringing-induced DRAs. The optimized apodization effectively eliminated the oscillatory side lobes in the PSF, thereby eliminating nearly all of the ringing effects. Specifically, the peak PSF side-lobe amplitude was suppressed from -13.2% for nonapodized PSF to -1.6% (i.e., an 8.3-fold reduction).

Results from in vivo studies clearly showed that the optimized radial imaging scheme can yield significant reductions in DRAs during the early myocardial enhancement phase of a FPP image series, where clinical interpretation of the DRA is most difficult. The quantitative artifact measurements (Fig. 7) show that the DRA width is on average slightly larger than 1 pixel along the PE line for Cartesian images. This is consistent with previous reports asserting that the DRA width for Cartesian imaging is typically one to two times the pixel width

along the PE line (10,56–58). In contrast, the DRA width measurements for the optimized radial images indicate that, on average, the estimated width of the signal loss was smaller than a third of a pixel width, which is negligible. The average in-plane resolution for Cartesian images was approximately $1.8 \times 2.8 \approx 5.0 \ mm^2$ and for radial images was $2.15 \times 2.15 \approx 4.6 \ mm^2$, which is slightly better than the parallel imaging–accelerated Cartesian scheme. It is clear that either method will not be capable of accurately resolving myocardial features that are smaller than $\approx 5 \ mm^2$ in area (roughly 2 mm along x and y for radial images). Nevertheless, the 2.15×2.15 mm^2 resolution achieved by the radial FPP method is considered relatively high among conventional FPP schemes that do not use advanced reconstruction methods and/or temporal acceleration [e.g., in the recent work by Motwani et al. (27), spatial resolution of the conventional SENSE-accelerated Cartesian method is $2.5 \times 2.5 \ mm^2$]. For all in vivo studies, we deliberately performed the radial scans as the first perfusion scan (before Cartesian), which may have disadvantaged the radial FPP scans in terms of the effect of residual contrast in potentially reducing DRAs for subsequent FPP scans.

In addition to ringing effects, there may be other potential contributing factors to the DRA as listed in the Introduction. Furthermore, it is difficult to decouple the contribution of each factor [e.g., motion versus ringing (19,59)]. Nevertheless, the left-to-right pattern of the observed DRAs in Cartesian images matches the PE direction (Fig. 6) and is consistent with described PSF ringing effects (Figs. 2b1, 3a1, and 5b1). Furthermore, the relatively low heart rates (rest scan), relatively small acquisition window (≈ 135 ms) and contrast dose (0.04 mmol/kg), all combined with short echo times (1.3–1.4 ms), alternating readout-direction radial acquisition, and local cardiac shimming should minimize the motion and susceptibility effects. All of these observations—in conjunction with our results and derivations—suggest that the main driver for reducing DRAs in our in vivo studies is elimination of the PSF ringing effects, achieved by using the optimized radial imaging scheme. It is worth mentioning that a similar apodization scheme (tapered weighting of k-space data) can also be applied to the other non-Cartesian (60) or even Cartesian (9) datasets to reduce the ringing effects; however, for Cartesian datasets, the apodization will reduce the already-low PE resolution to unacceptable levels.

Relation to Previous Work

Recent studies using high-resolution Cartesian imaging with temporally accelerated k-t schemes (24–27) have shown success in reducing DRAs by decreasing the spatial width of Gibbs ringing effects as compared with conventional Cartesian schemes. These results imply that Gibbs ringing is most likely a significant, if not the dominant, contributing factor to the DRA. However, achieving such resolutions (1.3–1.8 mm isotropic in-plane) with Cartesian imaging inevitably requires a high level of temporal acceleration, which has its own issues: the possibility of reduced temporal fidelity or loss of robustness due to modeling ("training data") assumptions (56,61)

especially with regard to breathing motion, and a need for specialized computational platforms. Furthermore, taking this approach, there is always the possibility that the images would still exhibit ringing-induced DRAs with a 1- to 2-pixel width [e.g., the mean DRA width for rest imaging was reported to be 1.3–2.7 mm by Maredia et al. (56)]. In contrast, our approach is based on sampling design and optimization of the PSF without a need for additional acceleration beyond conventional parallel imaging. Indeed, the imaging experiments in this work were performed using frame-by-frame reconstruction (i.e., without temporal acceleration). Moreover, we refrained from using highly accelerated (e.g., compressed sensing or nonlinearly regularized) reconstruction to achieve a fair comparison with the conventional Cartesian imaging scheme. However, incorporation of an edge-preserving regularized reconstruction scheme, such as 2D total variation regularization combined with radial SENSE, may improve the image quality.

Limitations

Our studies were limited to rest perfusion scans (maximum imaged heart rate = 78 beats per minute). Previous works have suggested that stress imaging is more prone to DRAs, which has been attributed to a higher degree of Gibbs ringing (7,10) and increased cardiac motion (19,59). The results of our phantom study suggest that, even for sharp signal-intensity discontinuities (6:1 ratio in Figure 5), the optimized radial imaging method effectively eliminated ringing-induced DRAs. Therefore, similar results (i.e., significantly reduced DRAs compared with Cartesian imaging) are expected for stress imaging. Lastly, although our results show that the proposed optimized radial imaging scheme is effective in reducing DRAs, the diagnostic accuracy of this approach in terms of detecting subendocardial ischemia remains to be tested in future work.

CONCLUSIONS

Based on a series of systematic investigations, from theoretical and phantom experiments to in vivo studies, we demonstrated that optimized radial first-pass perfusion imaging with wide k-space coverage and a simple reconstruction method can effectively eliminate ringing-induced DRAs while providing equivalent resolution and similar image quality as conventional Cartesian imaging. The potential clinical benefits of the proposed approach remain to be evaluated in patients with known or suspected coronary artery disease.

REFERENCES

1. Nesto RW, Kowalchuk GJ. The ischemic cascade: temporal sequence of hemodynamic, electrocardiographic and symptomatic expressions of ischemia. Am J Cardiol 1987;59:23C–30C.
2. Atkinson DJ, Burstein D, Edelman RR. First-pass cardiac perfusion: evaluation with ultrafast MR imaging. Radiology 1990;174:757–762.

3. Wilke NM, Jerosch-Herold M, Zenovich A, Stillman AE. Magnetic resonance first-pass myocardial perfusion imaging: clinical validation and future applications. J Magn Reson Imaging 1999;10:676–685.

4. Jerosch-Herold M, Kwong RY. Optimal imaging strategies to assess coronary blood flow and risk for patients with coronary artery disease. Curr Opin Cardiol 2008;23:599–606.

5. Arai AE. Magnetic resonance first-pass myocardial perfusion imaging. Top Magn Reson Imaging 2000;11:383–398.

6. Kellman P, Arai AE. Imaging sequences for first pass perfusion—a review. J Cardiovasc Magn Reson 2007;9:525–537.

7. Gerber BL, Raman SV, Nayak K, Epstein FH, Ferreira P, Axel L, Kraitchman DL. Myocardial first-pass perfusion cardiovascular magnetic resonance: history, theory, and current state of the art. J Cardiovasc Magn Reson 2008;10:18.

8. Fenchel M, Helber U, Simonetti OP, Stauder NI, Kramer U, Nguyen C-N, Finn JP, Claussen CD, Miller S. Multislice first-pass myocardial perfusion imaging: comparison of saturation recovery (SR)-TrueFISP-two-dimensional (2D) and SR-TurboFLASH-2D pulse sequences. J Magn Reson Imaging 2004;19:555–563.

9. Di Bella EVR, Parker DL, Sinusas AJ. On the dark rim artifact in dynamic contrast-enhanced MRI myocardial perfusion studies. Magn Reson Med 2005;54:1295–1299.

10. Ferreira P, Gatehouse P, Kellman P, Bucciarelli-Ducci C, Firmin D. Variability of myocardial perfusion dark rim Gibbs artifacts due to sub-pixel shifts. J Cardiovasc Magn Reson 2009;11:17.

11. Jerosch-Herold M. Quantification of myocardial perfusion by cardiovascular magnetic resonance. J Cardiovasc Magn Reson 2010;12:57.

12. Algranati D, Kassab GS, Lanir Y. Why is the subendocardium more vulnerable to ischemia? A new paradigm. Am J Physiol Heart Circ Physiol 2011;300:H1090–H1100.

13. Camici PG, Crea F. Coronary microvascular dysfunction. N Engl J Med 2007;356:830–840.

14. Bugiardini R, Merz CNB. Angina with "normal" coronary arteries: a changing philosophy. JAMA 2005;293:477–484.

15. Doyle M, Weinberg N, Pohost GM, et al. Prognostic value of global MR myocardial perfusion imaging in women with suspected myocardial ischemia and no obstructive coronary disease: results from the NHLBI-sponsored WISE (Women's Ischemia Syndrome Evaluation) study. JACC Cardiovasc Imaging 2010;3:1030–1036.

16. Patel A, Epstein F, Kramer C. Evaluation of the microcirculation: advances in cardiac magnetic resonance perfusion imaging. J Nucl Cardiol 2008;15:698–708.

17. Klem I, Heitner JF, Shah DJ, et al. Improved detection of coronary artery disease by stress perfusion cardiovascular magnetic resonance with the use of delayed enhancement infarction imaging. J Am Coll Cardiol 2006;47:1630–1638.

18. Meyer C, Strach K, Thomas D, Litt H, Nähle CP, Tiemann K, Schwenger U, Schild HH, Sommer T. High-resolution myocardial stress perfusion at 3 T in patients with suspected coronary artery disease. Eur Radiol 2007;18:226–233.

19. Meloni A, Al-Saadi N, Torheim G, Hoebel N, Reynolds HG, De Marchi D, Positano V, Burchielli S, Lombardi M. Myocardial first-pass perfusion: Influence of spatial resolution and heart rate on the dark rim artifact. Magn Reson Med 2011;66:1731–1738.

20. Storey P, Chen Q, Li W, Edelman RR, Prasad PV. Band artifacts due to bulk motion. Magn Reson Med 2002;48:1028–1036.

21. Wolff SD, Schwitter J, Coulden R, et al. Myocardial first-pass perfusion magnetic resonance imaging: a multicenter dose-ranging study. Circulation 2004;110:732–737.

22. Ferreira P, Gatehouse P, Bucciarelli-Ducci C, Wage R, Firmin D. Measurement of myocardial frequency offsets during first pass of a gadolinium-based contrast agent in perfusion studies. Magn Reson Med 2008;60:860–870.

23. Barkhausen JR, Hunold P, Jochims M, Debatin JRF. Imaging of myocardial perfusion with magnetic resonance. J Magn Reson Imaging 2004;19:750–757.

24. Plein S, Ryf S, Schwitter J, Radjenovic A, Boesiger P, Kozerke S. Dynamic contrast-enhanced myocardial perfusion MRI accelerated with k-t sense. Magn Reson Med 2007;58:777–785.

25. Vitanis V, Manka R, Boesiger P, Kozerke S. Accelerated cardiac perfusion imaging using k-t SENSE with SENSE training. Magn Reson Med 2009;62:955–965.

26. Manka R, Vitanis V, Boesiger P, Flammer AJ, Plein S, Kozerke S. Clinical feasibility of accelerated, high spatial resolution myocardial perfusion imaging. JACC Cardiovasc Imaging 2010;3:710–717.

27. Motwani M, Maredia N, Fairbairn TA, Kozerke S, Radjenovic A, Greenwood JP, Plein S. High-resolution versus standard-resolution cardiovascular MR myocardial perfusion imaging for the detection of coronary artery disease. Circ Cardiovasc Imaging 2012;5:306–313.

28. Adluru G, Awate SP, Tasdizen T, Whitaker RT, DiBella EVR. Temporally constrained reconstruction of dynamic cardiac perfusion MRI. Magn Reson Med 2007;57:1027–1036.

29. Adluru G, McGann C, Speier P, Kholmovski EG, Shaaban A, DiBella EVR. Acquisition and reconstruction of undersampled radial data for myocardial perfusion magnetic resonance imaging. J Magn Reson Imaging 2009;29:466–473.

30. Otazo R, Kim D, Axel L, Sodickson DK. Combination of compressed sensing and parallel imaging for highly accelerated first-pass cardiac perfusion MRI. Magn Reson Med 2010;64:767–776.

31. Harris FJ. On the use of windows for harmonic analysis with the discrete Fourier transform. Proc IEEE 1978;66:51–83.

32. Gottlieb D, Shu C-W. On the Gibbs phenomenon and its resolution. SIAM Review 1997;39:644–668.

33. Kak AC, Slaney M. Principles of computerized tomographic imaging. Philadelphia: Society for Industrial Mathematics; 2001. 327 pp.

34. Sharif B, Dharmakumar R, LaBounty T, Shufelt C, Thomson L, Merz N, Berman DS, Li D. Projection imaging of myocardial perfusion: minimizing the subendocardial dark-rim artifact. J Cardiovasc Magn Reson 2012;14(Suppl 1):P275.

35. Liang Z-P, Lauterbur PC. Principles of magnetic resonance imaging: a signal processing perspective. New York: Wiley-IEEE Press; 2000. 414 pp.

36. Oppenheim AV, Schafer RW. Discrete-time signal processing. Upper Saddle River, NJ: Pearson Education; 2009. 1120 pp.

37. Pipe JG. Reconstructing MR images from undersampled data: data-weighting considerations. Magn Reson Med 2000;43:867–875.

38. Bracewell RN. The Fourier transform and its applications. 3rd ed. Boston: McGraw-Hill; 2000. 616 pp.

39. Lauzon ML, Rutt BK. Effects of polar sampling in k-space. Magn Reson Med 1996;36:940–949.

40. Bracewell RN, Thompson AR. The main beam and ring lobes of an east-west rotation-synthesis array. The Astrophysical Journal 1973;182:77–94.

41. Gottlieb D, Gustafsson B, Forssén P. On the direct Fourier method for computer tomography. IEEE Trans Med Imaging 2000;19:223–232.

42. Scheffler K, Hennig J. Reduced circular field-of-view imaging. Magn Reson Med 1998;40:474–480.

43. Coggins BE, Zhou P. Polar Fourier transforms of radially sampled NMR data. J Magn Reson 2006;182:84–95.

44. Sharif B, Dharmakumar R, LaBounty T, Shufelt C, Thomson LE, Merz NB, Berman DS, Li D. Eliminating dark-rim artifacts in first-pass myocardial perfusion imaging. J Cardiovasc Magn Reson 2013;15(Suppl 1):O3.

45. Lauzon ML, Rutt BK. Polar sampling in k-space: reconstruction effects. Magn Reson Med 1998;40:769–782.

46. Naylor DA, Tahic MK. Apodizing functions for Fourier transform spectroscopy. J Opt Soc Am A 2007;24:3644–3648.

47. Kim D, Cernicanu A, Axel L. B_0 and B_1-insensitive uniform T_1-weighting for quantitative, first-pass myocardial perfusion magnetic resonance imaging. Magn Reson Med 2005;54:1423–1429.

48. Kim D, Gonen O, Oesingmann N, Axel L. Comparison of the effectiveness of saturation pulses in the heart at 3T. Magn. Reson. Med. 2008;59:209–215.

49. Peters DC, Derbyshire JA, McVeigh ER. Centering the projection reconstruction trajectory: Reducing gradient delay errors. Magn Reson Med 2003;50:1–6.

50. Peters DC, Botnar RM, Kissinger KV, Yeon SB, Appelbaum EA, Manning WJ. Inversion recovery radial MRI with interleaved projection sets. Magn Reson Med 2006;55:1150–1156.

51. Song HK, Dougherty L. Dynamic MRI with projection reconstruction and KWIC processing for simultaneous high spatial and temporal resolution. Magn Reson Med 2004;52:815–824.

52. Block KT, Frahm J. Radial single-shot STEAM MRI. Magn Reson Med 2008;59:686–691.

53. Walsh DO, Gmitro AF, Marcellin MW. Adaptive reconstruction of phased array MR imagery. Magn Reson Med 2000;43:682–690.

54. Pruessmann KP, Weiger M, Bornert P, Boesiger P. Advances in sensitivity encoding with arbitrary k-space trajectories. Magn Reson Med 2001;46:638–651.

55. Applegate KE, Tello R, Ying J. Hypothesis testing III: counts and medians. Radiology 2003;228:603–608.

56. Maredia N, Radjenovic A, Kozerke S, Larghat A, Greenwood JP, Plein S. Effect of improving spatial or temporal resolution on image quality and quantitative perfusion assessment with k-t SENSE acceleration in first-pass CMR myocardial perfusion imaging. Magn Reson Med 2010;64:1616–1624.

57. Gebker R, Jahnke C, Paetsch I, Kelle S, Schnackenburg B, Fleck E, Nagel E. Diagnostic performance of myocardial perfusion MR at 3 T in patients with coronary artery disease. Radiology 2008;247:57–63.

58. Gebker R, Jahnke C, Manka R, Frick M, Hucko T, Kozerke S, Schnackenburg B, Fleck E, Paetsch I. High spatial resolution myocar-

dial perfusion imaging during high dose dobutamine/atropine stress magnetic resonance using k–t SENSE. Int J Cardiol 2011:1–6.

59. Sharif B, Dharmakumar R, Thomson LEJ, Bairey Merz CN, Berman DS, Li D. Motion-induced dark-rim artifact in first-pass myocardial perfusion MR: a controlled canine study. In Proceedings of the 20th Annual Meeting of ISMRM, 2012. p. 1149.

60. Salerno M, Kramer CM, Meyer CH. Myocardial perfusion imaging with variable density spiral trajectories. In Proceedings of the 18th Annual Meeting of ISMRM, 2010. p. 3624.

61. Hansen MS, Kozerke S, Pruessmann KP, Boesiger P, Pedersen EM, Tsao J. On the influence of training data quality in k-t BLAST reconstruction. Magn Reson Med 2004;52:1175–1183.